Draft version September 9, 2009
Preprint typeset using LaTeX style emulateapj v. 03/07/07

AN FE XXVI ABSORPTION LINE IN THE PERSISTENT SPECTRUM OF THE DIPPING LOW MASS X-RAY BINARY 1A 1744−361

Fotis P. Gavriil[1, 2], Tod E. Strohmayer[1], Sudip Bhattacharyya [3]

Draft version September 9, 2009

ABSTRACT

We report on *Chandra X-ray Observatory* (*CXO*) High-Energy Transmission Grating (HETG) spectra of the dipping Low Mass X-ray Binary (LMXB) 1A 1744−361 during its July 2008 outburst. We find that its persistent emission is well modeled by a blackbody ($kT \sim 1.0$ keV) plus power-law ($\Gamma \sim 1.7$) with an absorption edge at 7.6 keV. In the residuals of the combined spectrum we find a significant absorption line at 6.961±0.002 keV, consistent with the Fe XXVI (hydrogen-like Fe) 2 - 1 transition. We place an upper limit on the velocity of a redshifted flow of $v < 221$ km s^{-1}. We find an equivalent width for the line of 27^{+2}_{-3} eV, from which we determine a column density of $7\pm1\times10^{17}$ cm^{-2} via a curve-of-growth analysis. Using XSTAR simulations, we place a lower limit on the ionization parameter of $> 10^{3.6}$ erg cm s^{-1}. The properties of this line are consistent with those observed in other dipping LMXBs. Using *Rossi X-ray Timing Explorer* (*RXTE*) data accumulated during this latest outburst we present an updated color-color diagram which clearly shows that 1A 1744−361 is an "atoll" source. Finally, using additional dips found in the *RXTE* and *CXO* data we provide an updated orbital period estimate of 52±5 minutes.

Subject headings: line: identification — binaries: general — stars: individual(1A 1744−361) — stars: neutron — X-rays: binaries — X-rays: stars

1. INTRODUCTION

1A 1744−361 is a neutron star Low Mass X-ray Binary (LMXB) discovered by the *Ariel V* satellite (Davison et al. 1976; Carpenter et al. 1977). This source is a transient LMXB, and several outbursts have been observed with a number of missions, most notably the *Rossi X-ray Timing Explorer* (*RXTE*). In 2001 Emelyanov et al. (2001) discovered a burst from the direction of 1A 1744−361, however, it could not be unambiguously identified as a thermonuclear burst. The first thermonuclear (type I) burst from 1A 1744−361 was discovered by Bhattacharyya et al. (2006a) using *RXTE*. This type I X-ray burst exhibited a 530-Hz burst oscillation which provided a measurement of the neutron star's spin frequency. The burst also provided an upper limit of $d < 9$ kpc, under the assumption that its maximum luminosity could not exceed the Eddington luminosity for a 1.4-$M_\odot$ neutron star (Bhattacharyya et al. 2006a).

This source also shows regular incidents of intensity "dips" in its X-ray emission. According to Frank et al. (1987), such dips are produced by obscuring material associated with a structured accretion disk. Dips would only be visible for inclination angles $60° \lesssim i \lesssim 80°$ (Frank et al. 1987). In principle dips could occur every orbital cycle, however, because of variations in the obscuring material in the disk, the presence of dips often varies from cycle to cycle and from source to source. The dips observed in 1A 1744−361, as is the case for other dipping LMXBs, exhibit complex structure (see Bhattacharyya et al. 2006a, Fig. 4). By measuring the spacing between two closely spaced dip episodes observed by *RXTE*, Bhattacharyya et al. (2006a) estimated the orbital period of 1A 1744−361 to be ∼97 minutes, however these dip episodes were separated by a data gap, thus not precluding shorter orbital periods.

Narrow absorption features have been seen in the persistent emission of many "dipping" LMXBs. For example, XB 1916−053 (Boirin et al. 2004; Iaria et al. 2006), X 1624−490 (Parmar et al. 2002), 4U 1323−62 (Boirin et al. 2005). By far, the most prominent features are the Fe XXV (He-like) and Fe XXVI (H-like) lines. The ubiquity of narrow features in dipping LMXBs suggests that they are a property of all LMXBs, but are seen predominately in dipping LMXBs because their particular geometry is optimal for viewing them (Díaz Trigo et al. 2006; Boirin et al. 2005). These features allow one to probe the structure, dynamics, and evolution of the material surrounding the neutron star. Thus, the spectral properties of 1A 1744−361 are of great interest. Using *RXTE* data, Bhattacharyya et al. (2006b) found that the persistent spectrum of this source is well modeled by a Comptonized blackbody model (Bhattacharyya et al. 2006b), and they also found evidence of a broad (∼0.6 keV) iron emission feature at ∼6 keV and an iron absorption edge at ∼8 keV. *RXTE* is not sensitive to narrow spectral features given its coarse spectral resolution and large FOV, thus, during the July 2008 outburst of this source we triggered *Chandra X-ray Observatory* (*CXO*) Target-of-Opportunity observations for this purpose.

In § 2 we present our analysis of the *CXO* (§ 2.1) and *RXTE* (§ 2.2) data from 1A 1744−361. In § 2.1.1 we present high resolution spectra of the source in which we find a Fe XXVI absorption feature. In § 2.2.1 we present an updated Color-Color diagram, and in § 2.3 we describe how we used the new observations of dips to constrain the orbital period of the source. In § 3 we discuss our results.

[1] NASA Goddard Space Flight Center, Astrophysics Science Division, Code 662, Greenbelt, Maryland, 20771, USA
[2] CRESST; University of Maryland Baltimore County, Baltimore, Maryland, 21250, USA
[3] Department of Astronomy and Astrophysics, Tata Institute of Fundamental Research, Mumbai 400005, India

2. ANALYSIS

2.1. *CXO Observations*

During 1A 1744−361's last outburst in July 2008, we triggered three *CXO* ToO Observations. These observations are summarized in Table 1. In order to search for narrow absorption features such as those seen in other dipping LMXBs the data were taken with the High-Energy Transmission Grating (HETG Canizares et al. 2005) aboard *CXO*. The HETG consists of two arms, the High Energy Grating (HEG) and the Medium Energy Grating (MEG). The HEG is sensitive to photons in the 0.8−10 keV band with a resolving power of $E/\Delta E{\sim}1000$ at 1 keV, and the MEG is sensitive to photons in the 0.4−5.0 keV band with a resolving power of 660 at 0.8 keV. The gratings were operated with ACIS which enables separation of the individual diffraction orders, $m = \pm1, \pm2, \pm3$, and a nondispersed zeroth order image is also obtained. We inspected all dispersed orders, however, for our analysis we concentrated on the $|m| = 1$ data because its effective area is more than an order of magnitude greater than the other orders for both the MEG and the HEG. Data in the different orders can be combined, however they have different spectral and spatial responses and thus we avoided doing so, lest we smear out any narrow features.

2.1.1. *High Resolution Spectroscopy*

For each HETG arm and dispersed order we extracted a source and background spectrum starting from the level 2 events file. We then created a response matrix and ancillary response file for each arm and order following the standard *CXO* analysis threads. We then grouped the spectra so that there were no less than 60 counts per bin after background subtraction. We used `XSPEC`[4] v12.5.1 for subsequent spectral modeling. We fit the MEG data to a photoelectrically absorbed blackbody and power-law model. The MEG data was well fit by this model, and there were no significant deviations. We then analyzed the HEG data and fit the same spectral model with an absorption edge at ∼7.6 keV, because of the HEG's higher response to photons above 5 keV. For the HEG we ignored bins above 8 keV because of their diminished statistics. A photoelectrically absorbed blackbody+power-law+edge model fits well, see Table 1, however, the residuals showed a clear deviation from the model at 6.96 keV in the 5 July 2008 (Fig. 1 panel 1A and 1B) and 7 July 2008 (Fig. 1 2A and 2B) observations. There were no comparable deviations in the 6 July 2008 observation, however, a hint of the feature could be seen at 6.96 keV. We noticed that the feature was primarily in the $m = -1$ and not the $m = 1$ spectra, in principle the two should have comparable spectra, since they have comparable responses and effective areas in that energy range, however, dithering could affect the spectrum and smear out the feature, which is what we suspect happened to the order $m = 1$ spectrum. We do not believe the feature is an instrumental artifact because then it would be seen in all $m = -1$ HETG observation of 1A 1744−361.

In order to increase the signal-to-noise ratio of the feature we combined all three observations and their ancillary response files. The combined spectrum is displayed in Fig. 2, and the 6.96 keV feature can be clearly seen (Fig. 2, inset). In the combined spectrum the line is clearly resolved. Assuming that the line is broadened because of the thermal Doppler effects, then the line profile close to the peak should resemble a Gaussian:

$$\phi_G(E, kT) = \frac{1}{\sqrt{2\pi}\Delta E} \exp\left[-\frac{(E - E_i)^2}{2\Delta E^2}\right], \quad (1)$$

where E_i is the line energy of the ion, and the line width, ΔE, is given by,

$$\Delta E = E_i \left(kT/m_i c^2\right)^{1/2}, \quad (2)$$

here, m_i is the ion mass and kT is the kinetic temperature (see Rybicki & Lightman 1979). Fitting Eq. 1 times a normalization to the line profile we obtain a line energy of $E_i = 6.961 \pm 0.002$ keV and a standard deviation of $\Delta E = 15.5 \pm 2.3$ eV. The theoretical properties of the Fe XXV (He-like) and the Fe XXVI (H-like) lines, the most prevalent lines in dipping LMXB spectra, are listed in Table 2. These values were obtained from the online line finding list[5] provided by the `XSTAR` emission modeling package (Kallman & Bautista 2001). The peak energy is consistent with the Fe XXVI $n = 2 - 1$ transition, and according to Eq. 2, our measured line width corresponds to a kinetic temperature of $kT = 254 \pm 2$ keV. Using the difference between the observed, E_i, and rest

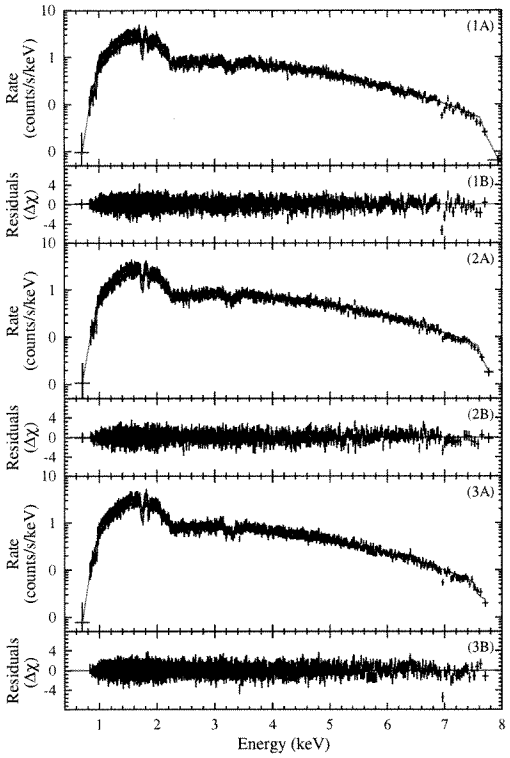

FIG. 1.— HEG order $m = -1$ spectra of 1A 1744−361. Panels 1A, 2A, and 3A corresponds to the 2008 July 5, July 6, and July 7 observation, respectively. The red curve represents the best fit spectral model, see Table 1 for details. Panels 1B, 2B, and 3B display the residuals, in terms of σ from the model, after fitting for the best-fit spectral model. Notice the highly significant deviations from the model at 6.961 keV in Panels 1B and 3B .

[4] http://xspec.gsfc.nasa.gov

[5] http://heasarc.gsfc.nasa.gov/docs/software/xstar/xstar.html

TABLE 1

Parameter[a]	2008 July 5	2008 July 6	2008 July 7	Total
Obs. ID	9884	9885	9042	...
Exposure (ks)	24.2	21.0	30.4	75.6
Count Rate (counts s^{-1})	4.9±0.02	4.86±0.02	5.02±0.02	4.927±0.009
Continuum Model				
N_H[b] ($\times10^{22}$ cm^{-2})	$0.40^{+0.03}_{-0.03}$	$0.35^{+0.03}_{-0.03}$	$0.44^{+0.03}_{-0.03}$	$0.414^{+0.006}_{-0.015}$
$E_{\rm Edge}$[c] (keV)	$7.56^{+0.08}_{-0.05}$	$7.73^{+0.01}_{-0.01}$	$7.699^{+0.013}_{-0.008}$	$7.645^{+0.006}_{-0.015}$
$\tau_{\rm Edge}$[d]	$1.8^{+0.3}_{-0.2}$	$3.5^{+1.3}_{-0.7}$	$3.5^{+1.3}_{-0.6}$	$1.17^{+0.10}_{-0.09}$
$kT_{\rm bb}$[e] (keV)	$0.98^{+0.08}_{-0.08}$	$1.05^{+0.11}_{-0.08}$	$1.09^{+0.07}_{-0.06}$	$1.06^{+0.02}_{-0.03}$
$R_{\rm bb}$[f] (km)	$4.8^{+0.8}_{-0.7}$	$4.4^{+0.7}_{-0.6}$	$4.4^{+0.4}_{-0.3}$	$4.3^{+0.2}_{-0.2}$
$L_{\rm bol}$[g] ($\times10^{36}$ erg s^{-1})	$2.6^{+0.3}_{-0.3}$	$3.0^{+0.6}_{-0.4}$	$3.5^{+0.5}_{-0.4}$	$3.1^{+0.2}_{-0.2}$
$\Gamma_{\rm PL}$[h]	$1.64^{+0.06}_{-0.06}$	$1.51^{+0.07}_{-0.05}$	$1.80^{+0.07}_{-0.06}$	$1.68^{+0.02}_{-0.02}$
Power-law Flux[i] ($\times10^{-9}$ erg cm^{-2} s^{-1})	$1.26^{+0.04}_{-0.04}$	$1.39^{+0.04}_{-0.06}$	$1.14^{+0.05}_{-0.06}$	$1.25^{+0.03}_{-0.02}$
Total Flux[j] ($\times10^{-9}$ erg cm^{-2} s^{-1})	1.399	1.368	1.241	1.367
$\chi^2_{\rm DoF}$ [DoF]	0.70 [1490]	0.69 [1333]	0.77 [1883]	0.83 [3407]
Fe XXVI line Properties				
E_i[k] (keV)	6.97±0.03	...	6.97±0.23	6.961±0.002
ΔE[l] (eV)	<50	...	< 229	15.5±2.4
W_E[m] (eV)	33^{+18}_{-15}	...	<40	27^{+2}_{-3}
FWHM[n] (km s^{-1})	<23192	...	< 5065	1613±21
N[o] ($\times10^{17}$ cm^{-2})	10^{+12}_{-6}	...	<13	$7.4^{+1.1}_{-1.0}$

[a] All errors represent 1-σ uncertainties.
[b] Hydrogen column density.
[c] Absorption edge energy threshold.
[d] Maximum depth of absorption edge at energy threshold.
[e] Blackbody temperature.
[f] Blackbody radius as determined from the normalization of the blackbody component and assuming a distance of d=9 kpc (the upper limit on the distance to the source).
[g] Bolometric luminosity as determined from the normalization of the blackbody component and assuming a distance of d=9 kpc (the upper limit on the distance to the source).
[h] Index of power-law component.
[i] Unabsorbed 2−10 keV flux of the power-law component.
[j] Unabsorbed 2−10 keV flux of the combined model.
[k] Line energy, see Eq. 1.
[l] Line width, see Eq. 1.
[m] Equivalent width of the line.
[n] FWHM of the line in units of velocity.
[o] Column density of the ion as determined by a COG analysis, see § 2.1.2 for details.

TABLE 2
THEORETICAL PROPERTIES[a] OF THE FE XXV (HE-LIKE) AND FE XXVI (H-LIKE) LINE.

Ion	E_0[b] (keV)	f[c]	A_{ul}[d] ($\times10^{14}$ s^{-1})
Fe XXV	6.70010	0.775	5.033
Fe XXVI	6.96614	0.408	2.863

[a] All parameters were provided by the XSTAR online line finding list http://heasarc.gsfc.nasa.gov/docs/software/xstar/xstar.html.
[b] Energy of transition.
[c] Oscillator strength.
[d] Einstein coefficient.

energy, E_0, of the line (see Table 2, we can determine the velocity of the absorbing material via $(E_i - E_0)/E_i = v/c$, for which we find $v < 221$ km s^{-1}. We can only place an upper limit of the flow velocity because the wavelength difference we measure ($\Delta\lambda = 0.001$ Å) is less than the absolute wavelength accuracy ($\Delta\lambda = 0.006$ Å) of the HEG, see the Chandra X-ray Center's Proposer's Observatory Guide[6].

[6] http://cxc.harvard.edu/proposer/POG/pog_pdf.html

2.1.2. *Curve-of-Growth Analysis*

A curve-of-growth (COG) analysis allows one to relate the equivalent width, W_E, of a spectral line to the column density, N, of the absorbing ion. XSPEC provides a function which computes the equivalent width of a line, for which we obtain $W_E = 27^{+2}_{-3}$ eV. To verify our XSPEC-measured equivalent width, we also computed the equivalent width analytically, by assuming that in the spectral region of interest the continuum is dominated by the power-law component. Our analytically determined equivalent width, 29.8 eV, was consistent with the value found using XSPEC.

In order to calculate the column density we computed theoretical COGs following Kotani et al. (2000) and Rybicki & Lightman (1979). The equivalent width, W_E, of the line is related to the optical depth, τ via

$$W_E = \int_0^\infty (1 - e^{-\tau}) dE, \quad (3)$$

here $\tau = Ns\phi$, where N is the column density, ϕ is the line profile shape, and

$$s = \pi f e^2 / m_i c. \quad (4)$$

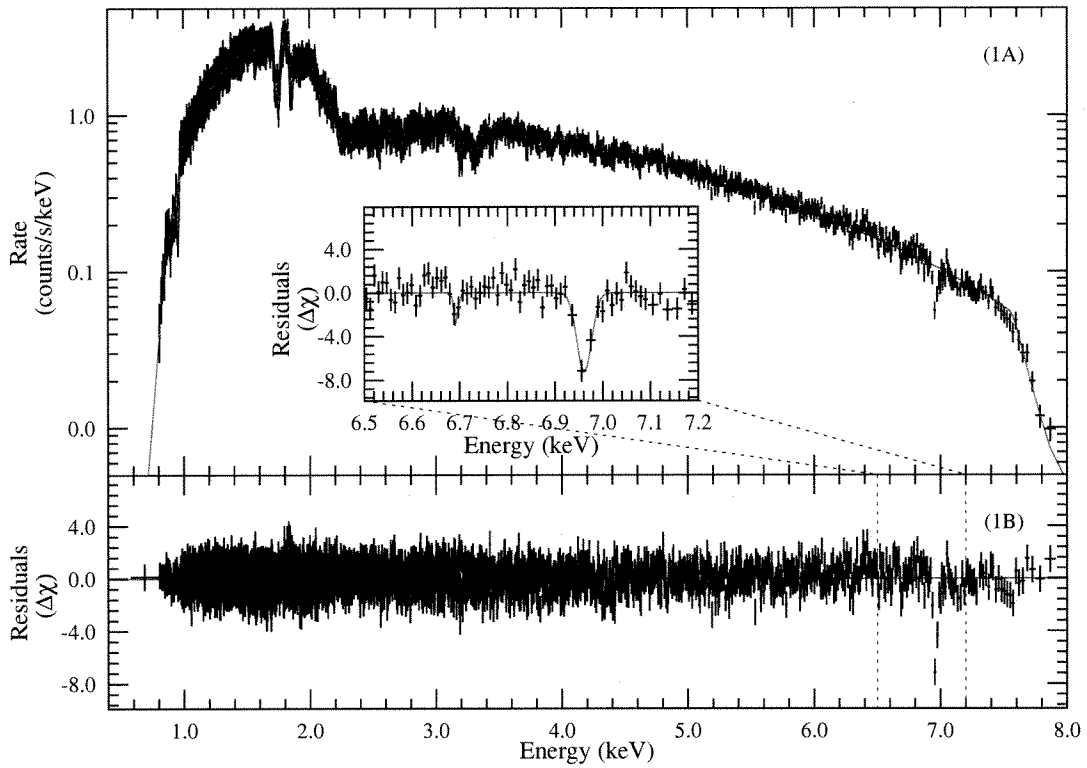

FIG. 2.— The sum of the three HEG $m = -1$ spectra of 1A 1744−361 displayed in Fig 1. The red curve is the best fit model (photoelectrically absorbed blackbody plus power law times an edge, see text for details). 1B: The residuals, in terms of σ from the model, after subtracting the best-fit model displayed in Panel 1B. Notice the highly significant deviations from the model at 6.961 keV corresponding to the Fe XXVI transition. Inset: An expanded view of the residuals around the Fe XXVI feature. The red curve is the best fit Gaussian line profile which has a centroid at $E_0 = 6.961 \pm 0.002$ keV with a width of $\Delta E = 15.5 \pm 2.3$ eV, see text for details. The Fe XXV is not statistically significant, however we fit for it in order to place an upper limit on its column density.

where f is the oscillator strength (see Table 2), and m_e and e is the electron mass and charge, respectively. Note, there is also a temperature dependent term in Eq. 4 which we ignored because Kotani et al. (2000) showed that the contribution of this term is negligible. The overall line profile, $\phi(E, kT)$ is found by convolving the line profile due to thermal broadening (ϕ_G, Eq. 1), and the line profile due to collisional broadening (ϕ_L), which has a Lorentzian profile, i.e,

$$\phi_L(E) = \frac{h\gamma}{4\pi^2(E - E_0)^2 + (h\gamma/2)^2}, \quad (5)$$

where γ is the sum of the Einstein coefficients, A_{ul}, over all lower energy states (see Table 2). Using the kinematic temperature found above, we then numerically integrated Equation 3 to obtain our COG which is displayed in Figure 3. Using the error on the dynamic temperature and the equivalent width we can obtain a confidence region for the Fe XXVI column density. We find $N_{\text{Fe XXVI}} = 7.4^{+1.1}_{-1.0} \times 10^{17}$ cm^{-2} for Fe XXVI.

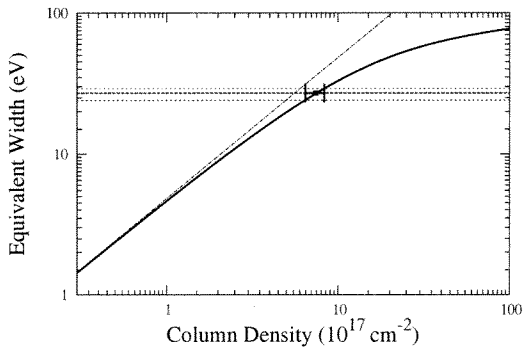

FIG. 3.— Curve-of-Growth (COG) for the Fe XXVI absorption line observed in the persistent emission of 1A 1744−361: Equivalent width versus column density for a kinematic temperature of $kT = 254$ keV. The error on the COG due to the error on the temperature would be smaller than the thickness of the line. The horizontal dashed line indicates the position of our measured equivalent width, and the dotted lines are the upper and lower bounds on the equivalent width. The dashed-dotted line represents the extrapolation of the "linear regime" of the COG .

2.1.3. *Ionization Parameter*

Although the presence of the Fe XXVI feature is clear, there was no discernible Fe XXV feature. However, an upper limit on the column density of the Fe XXV can constrain the ionization parameter

$$\xi = \frac{L}{n_e r^2}, \quad (6)$$

where L is the luminosity of the source, r is the distance from the central object to the absorber, and n_e is the electron number density. The electron number density, is related to the electron column density, N_e, via $n_e = N_e/\Delta r$, where Δr is the thickness of the absorbing slab. In order to measure the equivalent width of the Fe XXV transition, we fit for such a line using our combined spectrum, see Fig. 2 (inset). Then, using `XSPEC`, we measured the equivalent width in the same manner as for Fe XXVI. We then generated a COG for

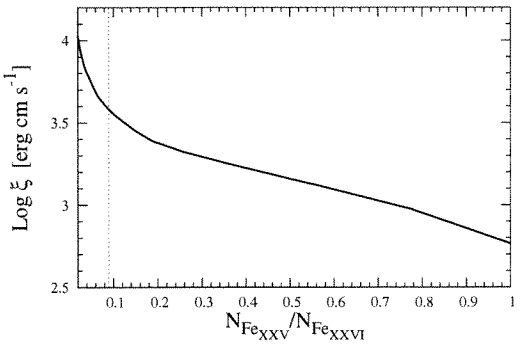

FIG. 4.— Ionization parameter, ξ, as a function of the relative abundance of Fe XXV to Fe XXVI as determined by our `XSTAR` simulations, see § 2.1.3 for details. The vertical dotted lines represents our upper limit on the relative abundance of Fe XXV to Fe XXVI which places a lower limit on the ionization parameter of $\xi > 10^{3.6}$ erg cm s^{-1} .

Fe XXV using the corresponding oscillator strength and Einstein coefficient (see Table 2). From our COG analysis we place an upper limit on the column density of Fe XXV of $N_{\rm Fe\ XXV} < 6.3 \times 10^{16}$ cm^{-2}. To calculate ξ we ran simulations of an ionized absorber using `XSTAR`. We assumed a spherical distribution of material and we used the standard spectral shape of a power-law with a spectral index of 2. We created a grid of ionization parameters and relative abundances using different initial choices for the electron density and luminosity. As an upper limit on the choice of luminosity we used the bolometric luminosity as measured from the blackbody component, $L < 3.5 \times 10^{36}$ erg s^{-1} (see Table 1). Our plot of ξ as a function of the ratio of the column density of Fe XXV to Fe XXVI is shown in Fig. 4. Given that the relative abundance of Fe XXV to Fe XXVI is less than 0.09, this places a lower limit on the ionization parameter of $\xi > 10^{3.6}$ erg cm s^{-1}.

2.2. *RXTE Observations*

The high time resolution data presented here were obtained from the Proportional Counter Array (PCA) aboard *RXTE*. The PCA is made up of 5 independent proportional counter units (PCUs). Each PCU is made up of three Xenon/Methane layers and an uppermost propane veto layer. The PCUs are sensitive to photons in the ∼2–60 keV band binned into 256 channels. The PCA and can time tag a photon to an accuracy of ∼1 μs. *RXTE* provides two standard data modes. `Standard-1` mode lightcurves with 0.125-s temporal bins and is summed over all spectral channels. `Standard-2` data provides lightcurves with 16-s time bins and is grouped into 129 spectral channels. As well as the standard modes, there are several user selected modes available. The ones used here include `GoodXenon` and `Event` mode. `GoodXenon` mode provides the full temporal and spectral resolution. `Event` mode data provides high-time resolution but often at slightly lower time resolution than `GoodXenon`, and the spectral channels are grouped using different grouping schemes, but often preserving 64 spectral channels.

2.2.1. *Color-Color Diagram*

We created a color-color diagram using the `Standard-2` data. Each PCU has different energy response, and PCUs 0 and 1 have lost their veto propane layer. PCU 2 is the most reliable, thus in our analysis we used only photons from the top Xenon layer of PCU 2. For count rates below 20 counts/s we used 2048-s long intervals, for count rates between 20 and 40 we took 512-s long intervals, and for the highest count rates we used 256-s long time intervals. For each spectrum we generated a model background using the `FTOOL pcabackest`. We defined our colors as follows: our soft color is the ratio of counts in the 2.30−3.54 keV band to that in the 5.19−3.54 keV band, and our hard color is defined as the ratio of the counts in the 5.19−8.52 keV band to that in the 8.52−17.74 keV band. Our color-color diagram is displayed in Fig. 5. In Bhattacharyya et al. (2006b) the authors reported that the source exhibited atoll-like behavior, however a Z-source track could not be unambiguously ruled out. The additional *RXTE* data presented here clearly display atoll source behavior.

2.2.2. *Timing Analysis*

Bhattacharyya et al. (2006a) reported a tentative (2.3 σ detection) of an 800-Hz quasi-periodic oscillation (QPO) for 1A 1744−361. Using all the available *RXTE* event data of 1A 1744−361, we searched for low-frequency and kHz QPOs. In our search we broke up our lightcurves into 250 s intervals. We found no highly significant ($\gg$ 3-σ) QPOs. The most significant QPO we found was a low frequency QPO at 29 Hz QPO for an observation on 2008 July 17 (Obs. ID 93155-01-06-03) at a significance of 3.0 σ.

In the *RXTE* archive we find a total of three thermonuclear bursts from 1A 1744−361. These bursts are displayed in Figure 6. The first burst occurred on 2005 July 16 (obs. ID 91050-05-01-00) and was first reported by Bhattacharyya et al. (2006a). This burst is the brightest observed from this source thus far (see Fig. 6 Panel A). Using its luminosity Bhattacharyya et al. (2006a) placed an upper limit on the distance to the source of d <9 kpc. The second and third bursts occurred on 2008 June 24 and 2008 July 25, respectively (see Fig. 6 Panels B and C). Bhattacharyya et al. (2006a) had found a significant burst oscillation in the first burst. We searched the other bursts for burst oscillations but found no comparable signals.

2.3. *Dip Timing Analysis*

In an attempt to constrain the orbital period of 1A 1744−361, we studied the dips of this 1A 1744−361. There were 11 independent dip episodes in the *RXTE* archive, where a dip episode comprises of a single dip or a cluster of closely spaced dips. A single short (∼2 s) dip was also observed in the 5 July 2008 *CXO* observation. Using two closely spaced dip episodes, Bhattacharyya et al. (2006a) were able to estimate the orbital period of 1A 1744−361 as 97±22 minutes. However, these dip episodes were separated by a data gap, thus not precluding a shorter period.

In order to establish whether the period found by Bhattacharyya et al. (2006a) is consistent with the additional dips, we performed the following analysis. We generated an array of sine waves with periods between $P = 3$ and $P = 94$ minutes in steps of 10^{-4} minutes. Assuming that dips only occur in a particular range of orbital phase, we

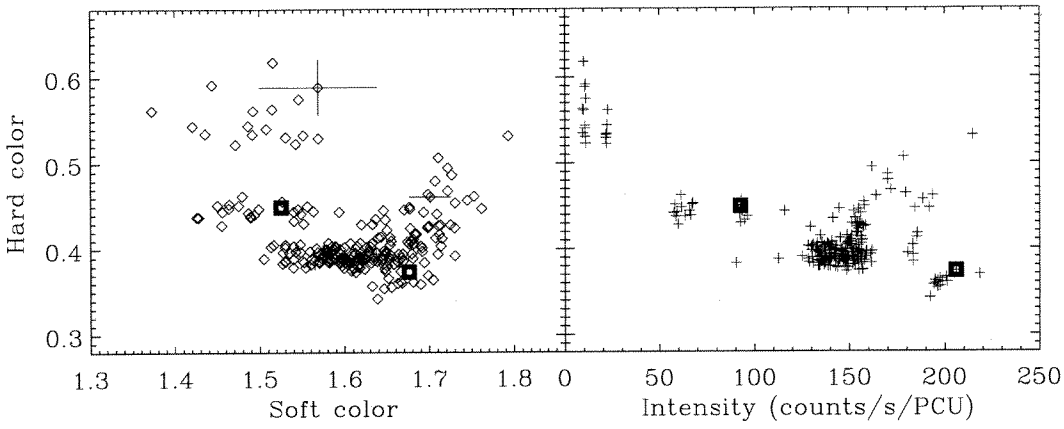

FIG. 5.— Color-Color diagram of 1A 1744−361 as observed by *RXTE*. Left: Hard color versus Soft color, see §2.2.1 for details. Right: Hard color versus Intensity. From both panels notice that 1A 1744−361 exhibits atoll-like behavior.

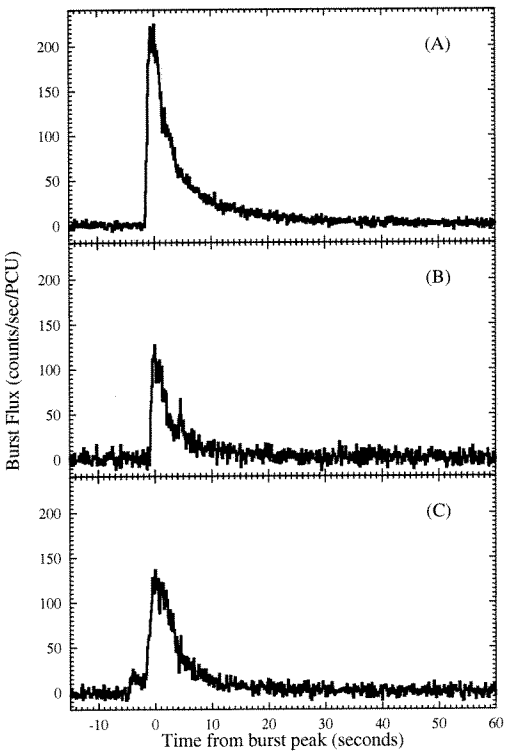

FIG. 6.— The thermonuclear X-ray bursts observed from 1A 1744−361 with *RXTE*. The lightcurves are background subtracted 0.125-S lightcurves generated using the full PCA energy band. The bursts were observed on 2005 July 16 (A), 2008 June 24 (B), and 2008 July 25 (C).

determined which of the sine waves satisfy the following conditions for all dip episodes: The center of all the dip episodes has to be within 0.2 cycles of the crest of the sine wave, and the 0.2 cycles around the trough of the sine wave could not contain a dip-free interval. This yielded 509 sine waves with orbital periods in our range that satisfied the above conditions. We then grouped these remaining permissible orbital periods into a histogram of bin size 1.8 minutes. The histogram is shown in Figure 7. Notice that the orbital period found by Bhattacharyya et al. (2006a) is not ruled out, however, the observations seem to favor roughly half that period. The mean of

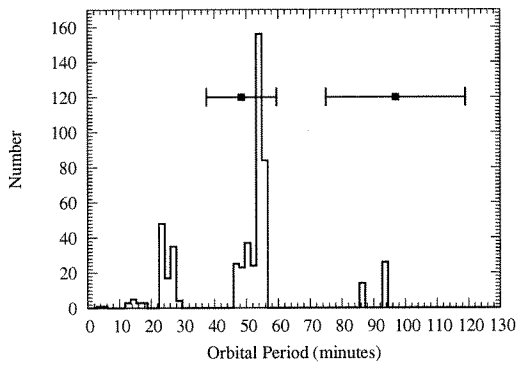

FIG. 7.— Histogram of orbital periods that ensure that dips episodes occur at the same orbital phase to within ±0.2 cycles. We stepped through orbital periods between 3 and 120 minutes in steps of 10^{-4} minutes. The ordinate shows the number of periods, grouped into 1.8 minute bins, that satisfied the conditions we set out in § 2.3. The interval centered on 97 minutes shows the interval derived by Bhattacharyya et al. (2006a). Our timing analysis shows that the most likely orbital period is 52±5 minutes, which agrees within the uncertainties with half the orbital period derived by Bhattacharyya et al. (2006a) (the interval centered on 48.5).

the distribution displayed in Figure 7 is 52 minutes and its standard deviation is 5 minutes. Thus we refine the orbital period estimate of this source to 52±5 minutes.

3. DISCUSSION

Using three pointed *CXO* HETG observations of 1A 1744−361 during its latest outburst we have discovered a significant 6.961 keV absorption feature in its persistent spectrum. The 6.961 keV absorption feature was present in the first and third *CXO* observation, and is well resolved in the combined spectrum. We have identified this feature as the Fe XXVI (hydrogen-like Fe) 2 - 1 transition . We find no evidence for lines due to other transitions. This is the first time such a narrow absorption feature has been observed in the spectrum of 1A 1744−361, making this source another example of a dipping LMXB which shows narrow absorption features. Because of the ubiquity of these features, it has been suggested that all LMXBs should exhibit them and that they are predominately observed from dipping LMXBs because their relatively edge on geometry facilitates such measurements (Díaz Trigo et al. 2006; Boirin et al. 2005).

Our discovery of such a feature in this dipping LMXB definitely corroborates that hypothesis.

The feature we have detected is consistent with the wavelength of the Fe XXVI $n = 2 - 1$ transition to the wavelength accuracy of the detector. We place an upper limit on the velocity of a redshifted flow of $v < 221$ km s^{-1}. In the combined spectrum, the line is well resolved, and we measure a line width of $\Delta E = 15.5 \pm 2.3$ eV. Under the assumption that the line is broadened due to thermal effects, the measured line width corresponds to a dynamic temperature $kT = 254 \pm 2$ keV. Using this temperature we performed a curve-of-growth analysis for Fe XXVI and determined a column density for Fe XXVI of $N_{\rm Fe\,XXVI} = 7.4^{+1.1}_{-1.0} \times 10^{17}$ cm^{-2}. This column density is comparable to that found for other dipping LMXBs. For example, for XB 1916−053 Iaria et al. (2006) found $N_{\rm Fe\,XXVI} = 6.6 \times 10^{17}$ cm^{-2}. We note however, that they used the linear approximation of the COG, i.e., for low column densities Equation 3 reduces to $W_E \approx (\pi f e^2/hm_i c)N$. However from Fig. 3 our features appears to lie beyond the linear regime. Unlike XB 1916−053 we do not find statistical evidence for a feature at the Fe XXV energy, indicative of the presence of a highly ionized absorber for 1A 1744−361. Our upper limit on the equivalent width on an underlying Fe XXV feature places a lower limit on the ionization parameter of $\xi > 10^{3.6}$ erg cm s^{-1}, as determined by our `XSTAR` simulations. We can not state with certainty that 1A 1744−361 is more highly ionized than other dipping LMXBs where both the Fe XXV and Fe XXVI are present because our lower limit on ξ is not above the values found for those sources, in particular XB 1916−053 and 4U 1323−62 which had $\log \xi = 4.15$ and $\log \xi = 3.9$, respectively (Iaria et al. 2006; Boirin et al. 2005).

1A 1744−361 is a prolific dipper, we have identified a total of 11 dips episodes in the *RXTE* data and 1 in the *CXO* data. Bhattacharyya et al. (2006a) determined an orbital period of 97±22 minutes from two consecutive dip episodes, however a data gap made it uncertain whether this was the true orbital period or a multiple thereof. In § 2.3 we propose that if the dips occur within a particular range of orbital phases, then the source's orbital period is more likely to be near half the value reported by Bhattacharyya et al. (2006a), specifically $P = 52 \pm 5$ min. Some of 1A 1744−361's dips, as observed by *RXTE*, are long and exhibit a great deal of structure, see Fig. 4 of Bhattacharyya et al. (2006a), for example. Unfortunately, in our *CXO* observations we observed a single short (2-s long) dip. With additional data from imaging telescopes such as *CXO*, it would be interesting to compare the spectral properties of 1A 1744−361 during dipping and non-dipping intervals. Variations in the properties of any observed narrow absorption lines would provide information about the structure and evolution of the material around the neutron star. Such an analysis was possible for 4U 1323−62, for which Boirin et al. (2005) found that the ionization parameter of 4U 1323−62 varied between dipping and non-dipping intervals.

In PCA data of 1A 1744−361 Bhattacharyya et al. (2006b) discovered a broad (0.6 keV) Fe emission line at 6 keV. The fact that this feature was below 6.4 keV prompted Bhattacharyya et al. (2006b) to predict that there might be an absorption feature at ∼7 keV that was unresolved due to *RXTE*'s course spectral resolution. No broad emission feature were observed in the individual or combined *CXO* observations, however this could be due to the smaller area of *CXO* as compared to *RXTE*. By combining additional observations one may be able to observe both the Fe emission feature and the Fe XXVI feature in 1A 1744−361. Indeed, such a measurement was made for 4U 1323−62 by Boirin et al. (2005), using *XMM-Newton*. If future high spectral resolution observations of 1A 1744−361 reveal such an emission feature, and it is relativistically broadened, then such measurements can potentially constrain the compactness of the star.

4. CONCLUSIONS

We present *CXO* HETG observations of 1A 1744−361 during its latest outburst, in which we have discovered a significant absorption feature at 6.961±0.002 keV in its persistent emission. We identify this feature as a Fe XXVI line, analogous to those seen in other dipping LMXBs. The width of the line was found to be $\Delta E = 15.5 \pm 2.4$ eV, which corresponds to a dynamic temperature of $kT = 254 \pm 2$ keV. We place an upper limit on the velocity of a redshifted flow of $v < 221$ km s^{-1}. The line had an equivalent width of $W_E = 27^{+2}_{-3}$ eV, for which we find a column density of $N_{\rm FeXXVI} = 7 \pm 1 \times 10^{17}$ cm^{-2} via a COG analysis. We place an upper limit on the ionization parameter of $\xi < 10^{3.6}$ erg cm s^{-1}. All these values are consistent with the Fe XXVI features seen in other dipping LMXBs. Using additional *RXTE* data we generated an updated color-color diagram for the source, which confirms the suggestion of Bhattacharyya et al. (2006b) that this source is an "atoll" source. We report two bursts in addition to the one reported by Bhattacharyya et al. (2006a). Performing a "dip" timing analysis, and under the assumption that dips only occur at a particular range of orbital phases, we find that $P = 52 \pm 5$ minutes is the most likely orbital period, nearly half the frequency found by Bhattacharyya et al. (2006a). 1A 1744−361 has demonstrated many of the properties of a canonical dipper, however, because it not as well sampled as the others, many of its parameters remain unconstrained. Further observations with *RXTE* and *CXO* during its next outburst are definitely warranted.

We thank C. B. Markwardt for useful discussions and for providing support for his numerical integration algorithm. This work has been supported by NASA via an ADP grant and a *Chandra* Guest Observer grant, as well as by the National Science Foundation (US NSF grant AST 0708424). This research has made use of data obtained through the High Energy Astrophysics Science Archive Research Center Online Service, provided by the NASA/Goddard Space Flight Center.

REFERENCES

Bhattacharyya, S., Strohmayer, T. E., Markwardt, C. B., & Swank, J. H. 2006a, ApJ, 639, L31

Bhattacharyya, S., Strohmayer, T. E., Swank, J. H., & Markwardt, C. B. 2006b, ApJ, 652, 603

Boirin, L., Méndez, M., Díaz Trigo, M., Parmar, A. N., & Kaastra, J. S. 2005, A&A, 436, 195
Boirin, L., Parmar, A. N., Barret, D., Paltani, S., & Grindlay, J. E. 2004, A&A, 418, 1061
Canizares, C. R., Davis, J. E., Dewey, D., Flanagan, K. A., Galton, E. B., Huenemoerder, D. P., Ishibashi, K., Markert, T. H., Marshall, H. L., McGuirk, M., Schattenburg, M. L., Schulz, N. S., Smith, H. I., & Wise, M. 2005, PASP, 117, 1144
Carpenter, G. F., Eyles, C. J., Skinner, G. K., Wilson, A. M., & Willmore, A. P. 1977, MNRAS, 179, 27P
Davison, P., Burnell, J., Ives, J., Wilson, A., & Carpenter, G. 1976, IAU Circ., 2925, 1
Díaz Trigo, M., Parmar, A. N., Boirin, L., Méndez, M., & Kaastra, J. S. 2006, A&A, 445, 179
Emelyanov, A. N., Aref'ev, V. A., Churazov, E. M., Gilfanov, M. R., & Sunyaev, R. A. 2001, Astronomy Letters, 27, 781
Frank, J., King, A. R., & Lasota, J.-P. 1987, A&A, 178, 137
Iaria, R., Di Salvo, T., Lavagetto, G., Robba, N. R., & Burderi, L. 2006, ApJ, 647, 1341
Kallman, T. & Bautista, M. 2001, ApJS, 133, 221
Kotani, T., Ebisawa, K., Dotani, T., Inoue, H., Nagase, F., Tanaka, Y., & Ueda, Y. 2000, ApJ, 539, 413
Parmar, A. N., Oosterbroek, T., Boirin, L., & Lumb, D. 2002, A&A, 386, 910
Rybicki, G. B. & Lightman, A. P. 1979, Radiative Processes in Astrophysics (New York: Wiley)